Drag on a circular intruder traversing a shape-heterogeneous granular mixture

Bitang Kwrung Tripura, Sonu Kumar,[*] Vamsi Krishna Reddy Anyam,[†] and K. Anki Reddy[‡]
Department of Chemical Engineering, Indian Institute of Technology, Guwahati 781039, Assam, India

(Received 27 July 2021; revised 11 February 2022; accepted 2 May 2022; published 7 July 2022)

The main aim of our work is to explore the effect of particle shape heterogeneity on the dynamics of an intruder moving through a two-dimensional mixture of dumbbells and disks. In spite of similar physical conditions (the mass of the dumbbell is the same as that of the disk) and the same area fraction, we noticed a significant difference in the drag experienced by the intruder as the mixture concentration varies. The propagation of stress from the intruder to the granular grains manifests in the form of force chains, and interestingly these force chains can vary significantly depending on the shape of the grains. These differences, however, appear to be suppressed in the frictionless case where the force chains cannot extend very far from the initial point of contact. Apart from particle shape, the effect of the area fraction of the system and the size of the intruder have also been explored. As the area fraction increases, the drag force on the intruder increases owing to the increase in the contact forces. Finally, we present the velocity and stress fields at different dumbbell fractions and for various intruder diameters to show the effect of the moving intruder on its surrounding particles.

DOI: 10.1103/PhysRevE.106.014901

I. INTRODUCTION

A large solid particle moving through a system of smaller particles has been a topic of interest due to its industrial applications such as mining and related activities. Moreover, because of the resemblance to the subsurface flows, it is finding applications in the field of sand locomotion of robots as well. These kinds of flows are still not completely understood due to the complex nature of the granular materials [1–3]. A prime focus in this type of flows is comprehending the drag characteristics on the larger solid particle or intruder due to the surrounding granular particles. The drag force on an intruder traversing granular media depends on various parameters such as the properties of the intruder, the external forces acting on it, and the geometry of the particles surrounding it.

The intruder properties such as its velocity and direction of motion significantly affect the drag experienced by it. For example, in a high-velocity regime, the drag force increases monotonically with the intruder's velocity [4], whereas in a low-velocity regime, it is independent of the intruder's velocity [5]. The drag force depends on not only the velocity of the intruder but also its direction of motion within the granular media: Liu *et al.* [6] noticed a higher drag when the intruder moves vertically downward than when it moves vertically upward in a gravity system. Surprisingly, the drag force is noticed [7] to depend weakly on the shape of the intruder (the cross section is the same for all shapes), at least for the set of intruders studied. A similar observation has been reported by Albert *et al.* [3] for a low-velocity regime.

In addition to the intruder properties, the drag force also depends on the external forces. For example, the drag is noticed [8–11] to be higher in a confined system than the one with a free surface, due to the presence of the confining pressure. Moreover, Zhou *et al.* [12] studied the motion of a cylindrical intruder through a compact bed of ceramic particles under high pressure to analyze the resistance offered by the particles on the intruder. In addition, the drag increases with an increase in the gravitational acceleration [13]. Even in a gravityless system, the drag was observed to increase with the square of the intruder's velocity [14]. As may be expected, the drag depends on the properties of the granular media surrounding it. For example, Zhou *et al.* [9] reported a higher drag on an intruder traversing a polydispersed granular media than a monodispersed one owing to their packing effects. The drag also depends on the shape of the granular particles. To this end, Zhou *et al.* [11] noticed that drag is more in a system of dumbbell-shaped granules than one of elliptical granules. Further, the authors noticed an increase in the drag with an increase in the aspect ratio of the ellipse particles. Most of the previous studies on intruder dynamics involved a system of spherical particles. However, in recent decades, understanding the dynamics of nonspherical particles [15–17] has garnered much interest in industrial and academic works. The reason is their relevance to practical applications, where the particles are usually mixtures of variegated shapes and sizes. A special case is a mixture [18,19] of spherical and nonspherical particles. To the best of our knowledge, there is hardly any work that has studied the characteristics of an intruder moving through a mixture of granular particles. In this regard, we probed the drag characteristics of an intruder moving through a mixture of disks and dumbbells in a two-dimensional gravityless system. The paper is organized as follows: in

[*]Current address: University of Notre Dame, South Bend, Indiana 46556, USA.
[†]Current address: Department of Chemical Engineering, Indian Institute of Science, Bangalore 560 012, India.
[‡]anki.reddy@iitg.ac.in

the next section, the simulation technique is explained, and in Sec. III the numerical results are reported along with our interpretations. Finally, Sec. IV summarizes our key findings.

II. SIMULATION METHODOLOGY

In this work we employed the discrete element method (DEM) [20] to study the dynamics of a moving intruder and its surroundings at different intruder sizes and at different system properties such as its area fraction and the fraction of dumbbells in it. To generate the initial configuration for a system at $\phi = 0.43$, first, we place the intruder of the required size at the origin and then generate particles one by one at random positions inside our system with enclosing walls at $y = \pm 3$ m. During the generation of the particle positions, if the newly created particle overlaps with any previously existing particle or the intruder or the wall, then this new particle is assigned to another randomly generated position using a uniform distribution. This procedure is repeated until we achieve the desired area fraction $\phi = 0.43$ (100 000 particles). Additionally, to incorporate polydispersity for both dumbbell and spherical particles, their sizes were also generated using a uniform distribution within the bounds of 10% polydispersity. The system is large enough that the effect of the seed of the random number generator becomes insignificant for our quantification. For a higher area fraction [$\phi = 0.77$ (180 000 particles), 0.82 (188 000 particles)] we followed a similar procedure as explained before; however, initially, the system dimension along the y direction is kept much larger than actually required. Then the y dimension is reduced by slowly moving the walls towards each other until the system reaches the required area fraction ϕ while the intruder is fixed at the origin. The system is then allowed to equilibrate till the total kinetic energy (KE) of the particles reaches KE $< 10^{-9}$ kg m^2/s^2. For ensuring that the area fraction is homogeneous throughout the system, the local area fraction is calculated along a grid of 0.01 m $\times$ 0.01 m to ensure homogeneity within 2%. If the system is not homogeneous, a new system is created. The mean diameter of disk particles is 0.01 m, while the dumbbells are constructed using two equally sized, nonoverlapping, and fused disk particles of mean diameter 0.007 m. This guarantees both disk and dumbbell particles to have equivalent mass on average, while a polydispersity of 10% avoids crystallization in the system. At time $t = 0$, the intruder is moved at a constant velocity V_i along the positive x direction for a total distance of 3 m. Note that periodic boundary conditions are applied in the x direction. Figure 1 shows an initial configuration of one of our simulation systems with the circular intruder having a diameter of 0.10 m placed at a distance of $h = 3$ m from the top wall.

In the DEM technique, the positions and velocities of each particle are updated at regular intervals by integrating the equations of motion using the velocity Verlet algorithm. In the equations of motion, only contact forces are considered since ours is a gravityless system. For computing the normal ($\boldsymbol{f}_{ij}^{n}$) and the tangential ($\boldsymbol{f}_{ij}^{t}$) components of the contact forces on particle i due to particle j, we adopt the contact force model

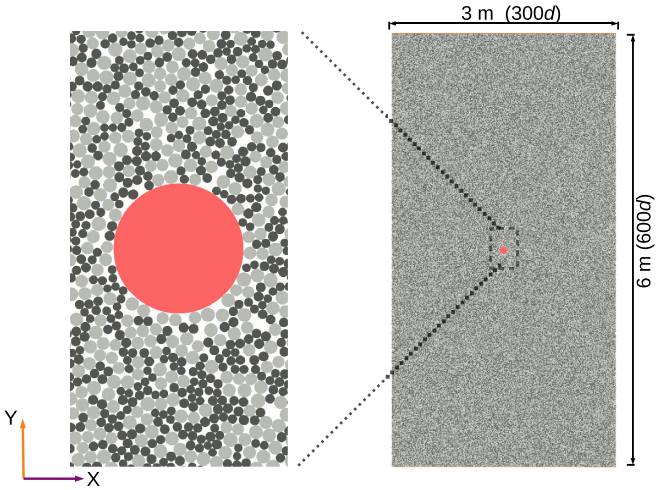

FIG. 1. One of the initial configurations showing the intruder placed at the center (taken as the origin) of our system. Our granular system consists of four different types of particles: a large intruder shown in red of diameter 0.1 m, granular disks represented by a lighter gray of diameter 0.01 m $\pm$ 10%, granular dumbbells represented by darker gray/black and created by gluing two equal disks of diameter $\sim$0.007 m $\pm$ 10%, and granular disks of diameter 0.01 m acting as the wall at $y = \pm 3.0$ m, represented by orange and frozen in place for the entirety of the simulation. Moreover, the mass density of all particles (mass/area) is set as 20 kg/m^2, and the average mass of disks and dumbbells is similar when averaged across the system. The x direction is kept periodic, and there is no gravity in any of the simulations. The full initial configuration is shown on the right, while the left panel shows a zoomed-in version near the vicinity of the intruder ($d = 0.01$ m is the average diameter of granular disks).

[21,22] as

$$\boldsymbol{f}_{ij}^{n} = \sqrt{\frac{d_i d_j}{2(d_i + d_j)}}\sqrt{\xi_{ij}}\left(k_n \xi_{ij}\hat{\boldsymbol{n}}_{ij} - m_{\text{eff}}\gamma_n \dot{\boldsymbol{r}}_{ij}^{n}\right), \tag{1}$$

$$\boldsymbol{f}_{ij}^{t} = -\sqrt{\frac{d_i d_j}{2(d_i + d_j)}}\sqrt{\xi_{ij}}\left(k_t \boldsymbol{\Delta s}_{ij} + m_{\text{eff}}\gamma_t \dot{\boldsymbol{r}}_{ij}^{t}\right). \tag{2}$$

Here d_i and d_j are the diameters and m_i and m_j are the masses of particles i and j, respectively. The normal spring constant $k_n = 2 \times 10^9$ (kg m^{-1} s^{-2}), the tangential spring constant $k_t = 2.456 \times 10^9$ (kg m^{-1} s^{-2}), and normal and tangential damping coefficients are $\gamma_n = \gamma_t = 8 \times 10^6$ (m s)$^{-1}$, respectively. The values of k_n and k_t were calculated with the Young's modulus of the particles, $E = 2$ G Pa, Poisson ratio $\nu = 0.3$, and density $\rho = 2000$ kg/m^3. The upper limit of $\boldsymbol{f}_{ij}^{t}$ is restricted to $\mu \boldsymbol{f}_{ij}^{n}$ for slipping between the contacts. Two coefficients of friction μ (0 and 0.5) were considered in the present study. $\hat{\boldsymbol{n}}_{ij}$ is the unit vector in the direction of the line joining the centers of the particles i and j. Two particles are said to be in contact if the overlap $\xi_{ij} \geqslant 0$. $\boldsymbol{\Delta s}_{ij}$ stands for the tangential displacement vector, and the normal and tangential relative velocities are represented by $\dot{\boldsymbol{r}}_{ij}^{n}$ and $\dot{\boldsymbol{r}}_{ij}^{t}$, respectively. Moreover, $m_{\text{eff}} = \frac{m_i m_j}{m_i + m_j}$ is the effective mass. The time step is set to 2×10^{-6} s. The run time for the simulation is calculated and adjusted to the time taken by the intruder to cover a distance of 3 m in the x direction at a given velocity.

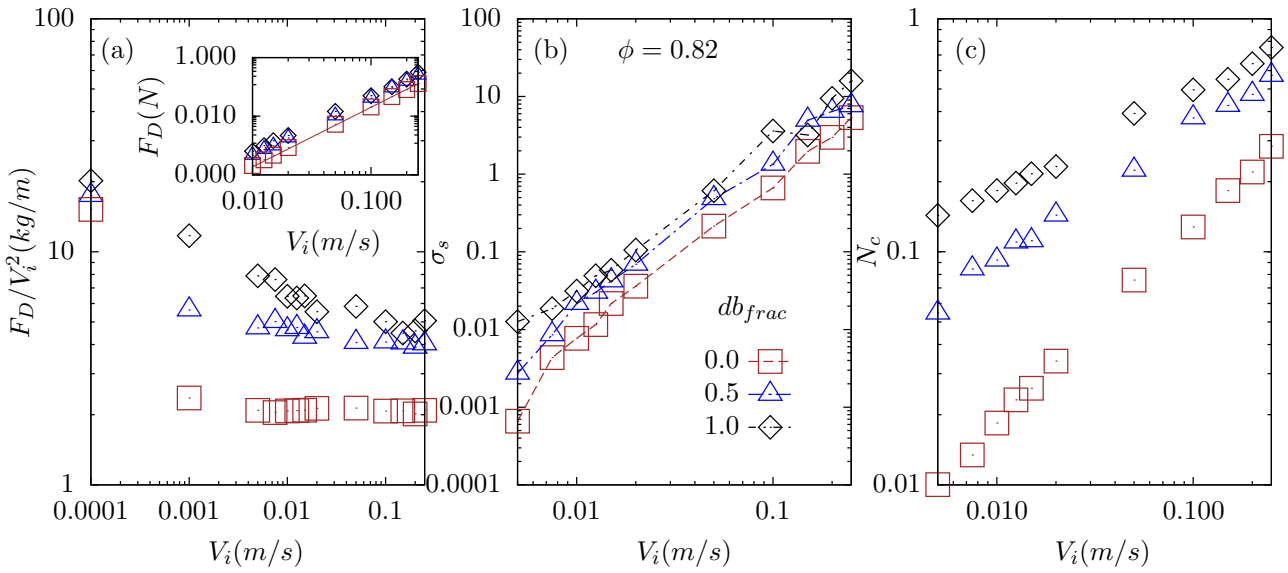

FIG. 2. (a) The time-averaged drag force F_D normalized by the square of intruder's velocity V_i, (b) the stress decline slope σ_s, and (c) the averaged number of particles in contact (N_c) as a function of intruder's velocity V_i for the fractions of dumbbells (db_{frac}) = 0, 0.5, and 1. The area fraction is $\phi = 0.82$, the coefficient of friction is $\mu = 0.5$, and the diameter of the intruder is $D_i = 0.05$ m.

The position and velocity of a dumbbell is its center of mass and its center of mass velocity. The total force and torque on a dumbbell are computed as the sum of the forces and torques on its constituent particles. All the simulations were performed using the LAMMPS [23] package, and OVITO [24] was used for visualization.

III. RESULTS AND DISCUSSION

In this section, we will present the numerical results for an intruder translating through a mixture of dumbbells and disks.

A. Dumbbell fraction

In this subsection, we studied the characteristics of a moving intruder and its surroundings at various mixture concentrations. To this end, we computed the drag force (F_D), the coordination number (N_c) of the intruder, and the stress decline slope (σ_s). In this work F_D and N_c correspond to their time-averaged values, and we note that the average doesn't include a few values at the beginning of the simulation to avoid initial intermittencies. In this subsection, the area fraction of the system is $\phi = 0.82$, the coefficient of friction is set to $\mu = 0.5$, and the diameter of the intruder is taken as $D_i = 5$ cm. At all fractions of dumbbells db_{frac}, the drag force F_D increases quadratically with an increase in the intruder's velocity V_i [see Fig. 2(a)]. A similar result has been noticed for an intruder placed inside a two-dimensional system of spherical granules [25]. However, at a very low intruder's velocity ($V_i \leqslant 0.01$), the drag force doesn't scale as V_i^2 for all the fractions of dumbbells. This is because, in a quasistatic regime ($V_i \leqslant 0.01$), the drag force is weakly dependent on the intruder's velocity. In this regime, the drag mainly depends on the heterogeneous distribution of stresses in the granular media [5]. As the intruder traverse granular media, a dense structure of particles evolves progressively in front of the intruder and then gets saturated [14]. This structure comprises particles that are interconnected through a network of contacts or force chains, and it is accompanied by the cyclic evolution and the breakage of force chains. The drag force on the intruder moving through a system of spherical particles is mainly due to the alternating evolution and buckling of force chains in the material and the interparticle friction [26]. At the same coefficient of friction, the drag force increases with an increase in the fraction of dumbbells db_{frac} [see inset of Fig. 2(a)]. This result can be attributed to a decrease in the frequency of force-chain buckling events with an increase in db_{frac}. This is due to an increase in the mutual resistance to the relative motion of the particles in contact, particularly the "a" type of contacts as shown in Fig. 3. Two types of contacts are possible between two particles if at least one of those is a dumbbell. In the first type, both parts of a dumbbell are simultaneously in contact with either disk or one part of another dumbbell [Fig. 3(a)], whereas in the second type, only one part of a dumbbell is in contact with a disk or one part of another dumbbell [Fig. 3(b)]. As the fraction of dumbbells increases, the chances of occurrence of the "a" type of contacts increases, resulting in an increase in the interlocking type of phenomena. This yields a decrease in the frequency

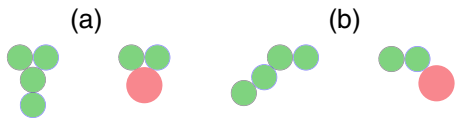

FIG. 3. The two possible types of contacts in a dumbbell-dumbbell or dumbbell-disk interaction. (a) The two parts of a dumbbell are simultaneously in contact with a disk or one part of another dumbbell. (b) Only one part of a dumbbell is in contact with a disk or one part of another dumbbell. Here the green ones represent dumbbells and the pink ones that of disks.

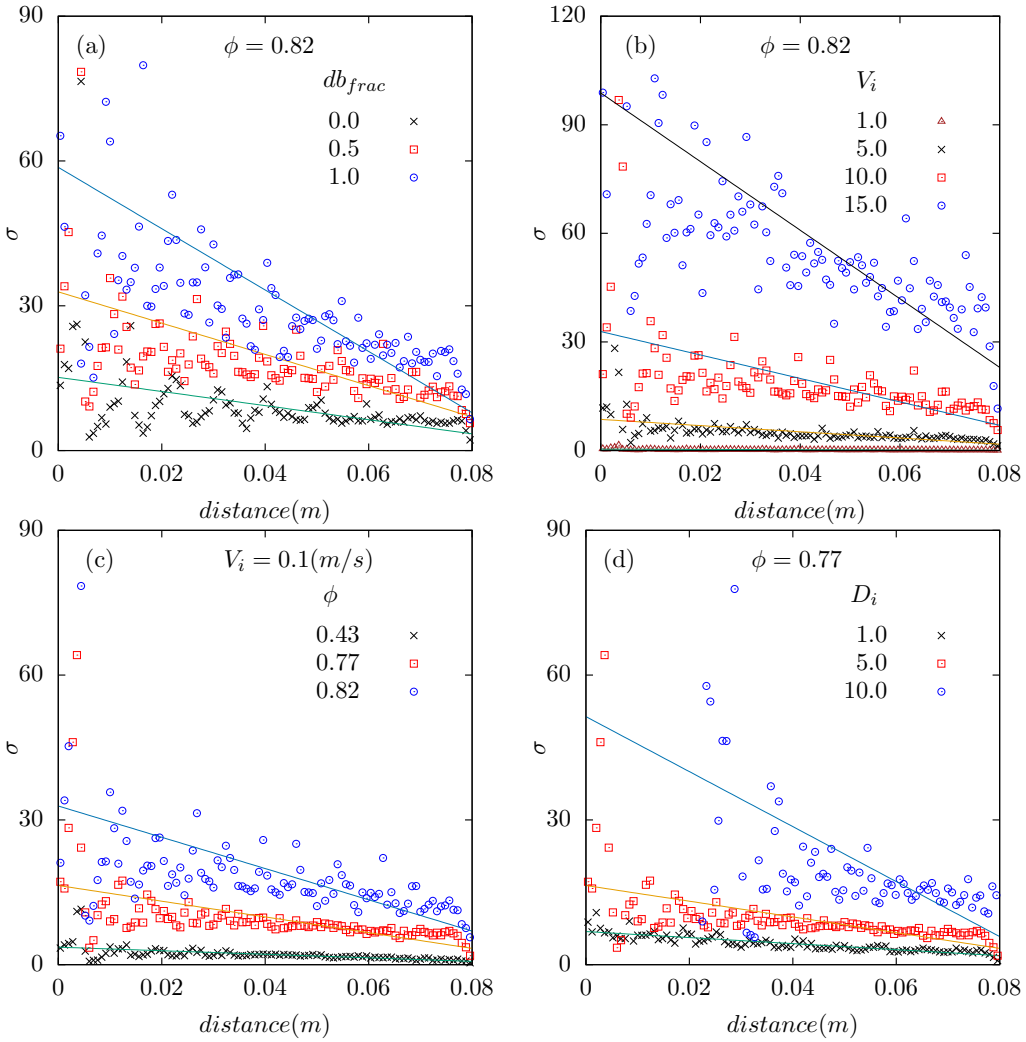

FIG. 4. The magnitude of stress σ as a function of distance from the intruder's front surface (a) for different dumbbell fractions db_{frac} and $\phi = 0.82$, (b) for different intruder velocities V_i with systems having $db_{frac} = 0.5$ and $\phi = 0.82$, (c) for different area fractions ϕ with systems having $db_{frac} = 0.5$ and at $V_i = 0.10$ m/s, and (d) for different intruder diameters (D_i) with $\phi = 0.77$. The coefficient of friction is $\mu = 0.5$ in all the cases, and the intruder diameter $D_i = 0.05$ m is in panels (a), (b), and (c).

of buckling events in the structure in front of the intruder or in other words an increase in the drag force on the intruder.

After analyzing the drag on the intruder, we studied its effect on the particles in front of it in terms of the magnitude of the stress decline slope σ_s. In a plot of the stress σ vs the distance from the intruder surface (shown in Fig. 4), σ_s is the slope of the line of best fit. The stress tensor σ_{ab} on the ith particle due to its N_p pairwise interactions is calculated as $\sigma_{ab} = \frac{1}{2\times A}\Sigma_{j=1}^{N_p}(r_{i_a}F_{i_b} + r_{j_a}F_{j_b})$ where a and b take on x and y values to produce the components of the stress tensor. Here r is the position of the particles, F is the force due to the pairwise interaction, and A is the area of the ith particle. The stress is calculated as $\sigma = -\frac{1}{2}(\sigma_{xx} + \sigma_{yy})$. Usually the stress is maximum in the region close to the intruder. The distance between the intruder surface and the region at which the stress is equal to the average stress of the system doesn't vary significantly due to a change in the properties of the system or the intruder. The reason for this is the absence of gravity. A higher σ_s indicates a higher stress near the intruder surface and a rapid decrease in stress as a function of the distance from the intruder surface. As the intruder velocity increases, σ_s increases because the intruder exerts more stress on the particles close to it [Fig. 2(b)]. Moreover, σ_s increases with an increase in the fraction of dumbbells. This behavior can be attributed to the interlocking type of phenomena that occurs with the dumbbell particles, which results in a higher stress close to the intruder. The drag force in the granular media arises from the particles in contact, and if the average force exerted by each contacting particle is constant, then the more the number of contacts, the greater the drag on the intruder. The increase in the number of contacts N_c with an increase in the intruder's velocity V_i as noticed in Fig. 2(c) is consistent with the drag force result. A similar result was observed previously for a system of disk particles [27]. As the fraction of dumbbells increases, the number of contacts N_c increases. This is due to a decrease in the frequency of buckling events in the region in front of the intruder because of the interlocking type of phenomena experienced by the dumbbells. We have also shown the similar analysis for systems with $\phi = 0.43$ and 0.77 in Figs. S1 and S2 in the Supplemental Material [28].

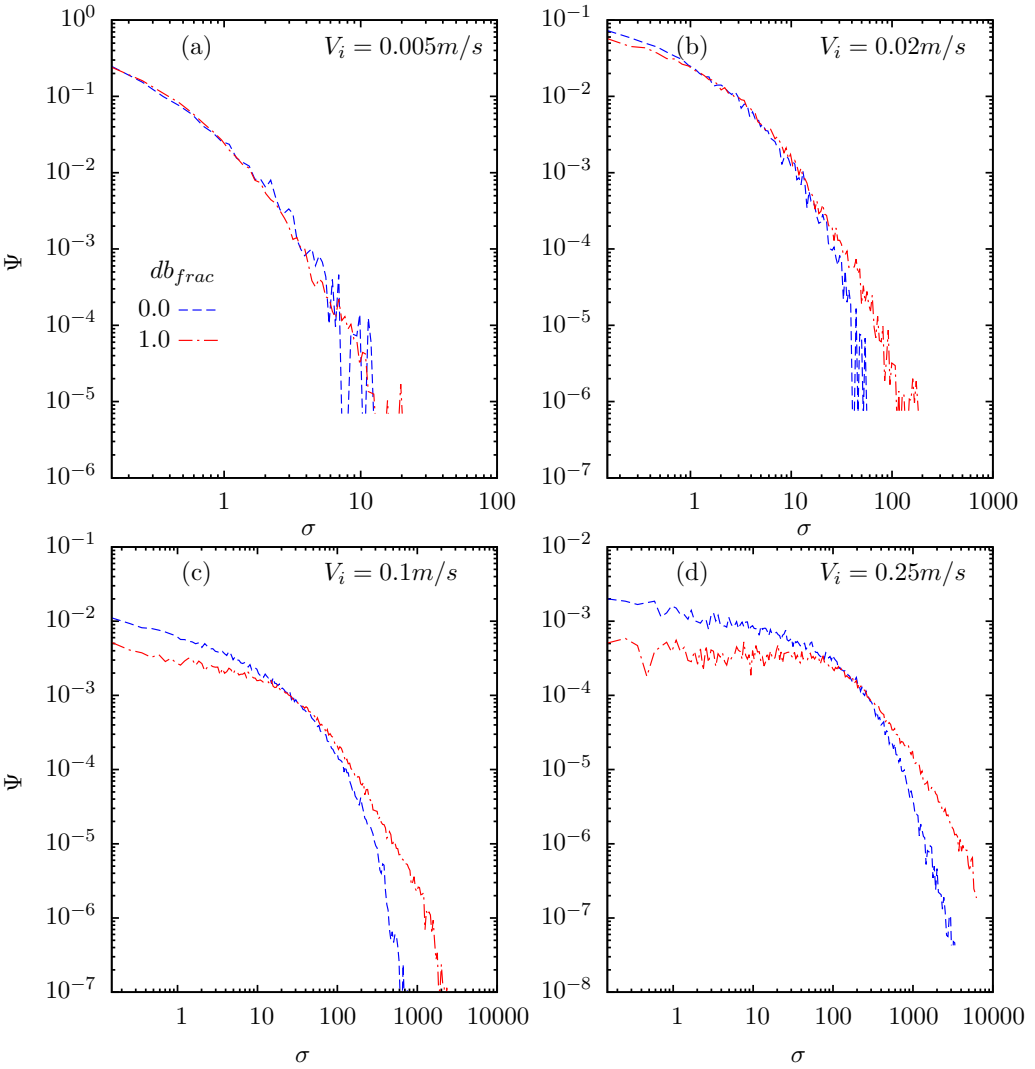

FIG. 5. The probability distribution function Ψ of the stress σ experienced by the intruder for four different velocities of the intruder V_i: (a) 0.005 m/s (b) 0.02 m/s (c) 0.1 m/s, and (d) 0.25 m/s. Here $db_{frac} = 0$ and 1 are the fraction of dumbbells in the system.

The probability distribution function (PDF) of stress experienced by the intruder at different fractions of dumbbells is studied to understand the effect of interlocking potential of dumbbells on the intruder (Fig. 5). Irrespective of the intruder's velocity, the stress is noticed to be higher in the case of dumbbells as compared to that of disks. This further justifies our claim regarding the interlocking type of phenomena noticed in a system involving dumbbell particles. The drag force on the intruder is due to the particle contacts around its entire periphery. Hence, we analyzed the number of contacts and their relative stress contributions at different angular positions on the intruder surface. Note that the stress mentioned above corresponds to the average normal stress, which is computed as $\sigma = -1/2(\sigma_{xx} + \sigma_{yy})$. In this regard, we displayed the stress distributions around it in Fig. 6 for $\phi = 0.82$ and $\mu = 0.5$. Note that the angular positions θ correspond to the region around the intruder, and they are computed concerning the center of the intruder. In both distributions, the angular positions ranging from 0° to 180° correspond to the region around the top half of the intruder, whereas the ones from 0° to -180° correspond to the lower half of the intruder where 0° is in front of the intruder and $\pm 180^\circ$ is at the rear end as shown in the inset of Fig. 6(f). As the intruder moves through the granular media, a wake is formed behind it for all the fractions of dumbbells, which can be noticed in $N_{c_\theta} = 0$ at $90^\circ < \theta < 180^\circ$ and $-180^\circ < \theta < -90^\circ$ in Figs. 6(a)–(c). Potiguar and Ding [4] reported the formation of the wake behind the intruder at high intruder velocities. However, in our work, we noticed the formation of wake even at velocities of the intruder as low as $V_i = 0.005$ m/s and for all fractions of dumbbells because of our system being a gravityless one. The particles colliding with the intruder are mainly confined to the front part of the intruder in the sense: $-90^\circ < \theta < 0^\circ$ and $0^\circ < \theta < 90^\circ$. The number of contacts at different angular positions increases with an increase in either the intruder's velocity or the fraction of dumbbells. This result is coherent with that of the average number of contacts as a function of the intruder's velocity as shown in Fig. 2(c). The averaged stress (P_θ) in the region around the intruder is confined to the angular positions between 0° and $\pm 90^\circ$ because particles lying only in this region collide with the intruder as noticed in the N_{c_θ}. At different θ, the averaged stress at each angular position

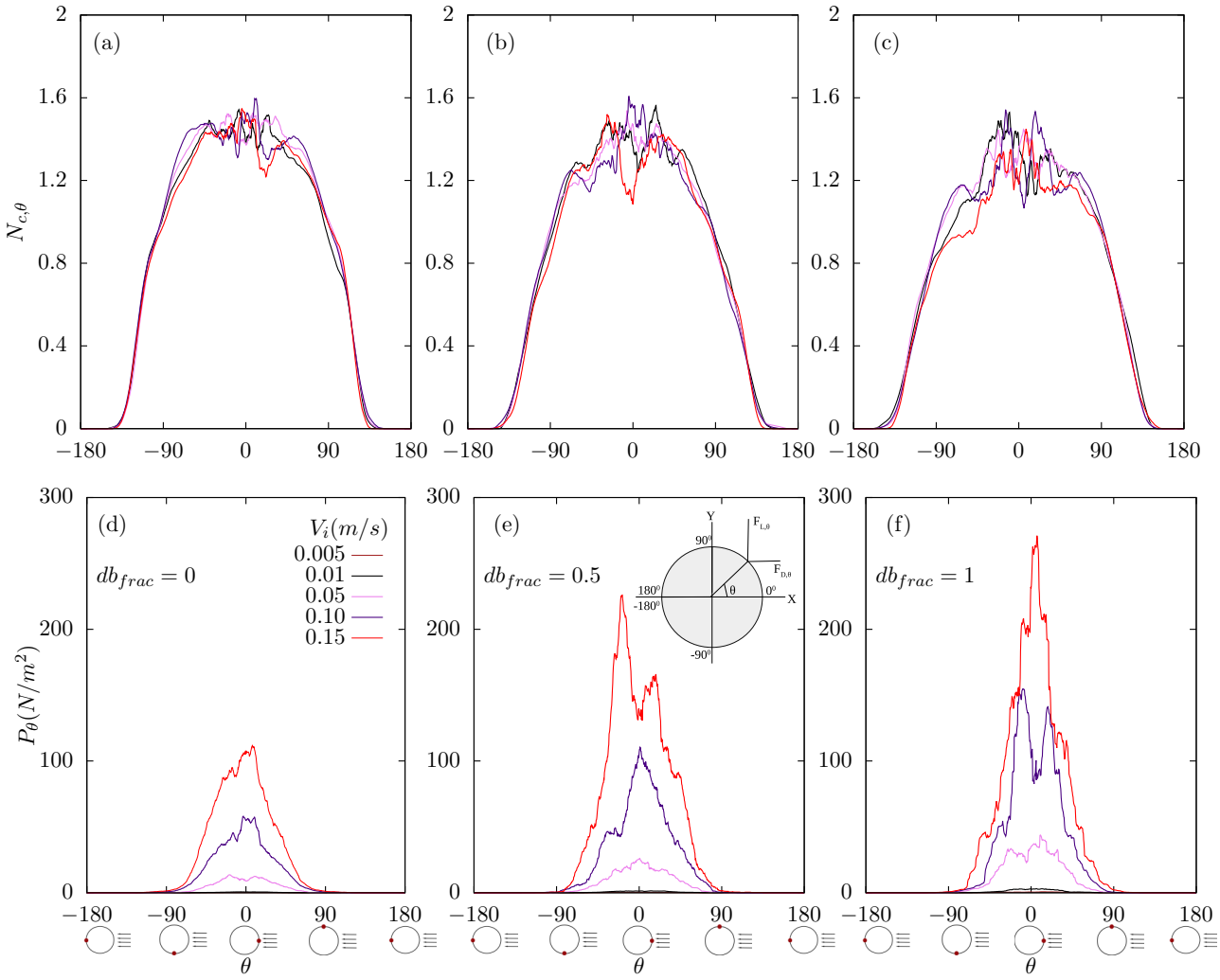

FIG. 6. The average number of particles in contact N_{c_θ} as a function of angular position (θ) for the fraction of dumbbells db_{frac} = (a) 0.0, (b) 0.5, and (c) 1.0. The average pressure P_θ as a function of angular position at different intruder velocities V_i for the fraction of dumbbells db_{frac} = (d) 0.0, (e) 0.5, and (f) 1.0. The coefficient of friction is $\mu = 0.5$, the area fraction is $\phi = 0.82$, and the inset in (e) displays how the angular positions are calculated around the intruder surface.

increases with an increase in the fraction of dumbbells. This result further justifies our claim that with an increase in the fraction of dumbbells there is an increase in drag in a frictional system. Apart from the interparticle friction, the geometry of the particles in front of the intruder also contribute to an increase in the stress or the drag force [11], whereas for the frictionless system, i.e., $\mu = 0.0$ (shown in Fig. S3 of the Supplemental Material [28]), the magnitude of drag force experience around the intruder surface does not vary much even with an increase in the fraction of dumbbells. To understand the sole effect of the geometry of the particles on the drag force experienced by the intruder, we study the same for the frictionless systems [11] at different fractions of dumbbells in the next subsection.

B. Absence of frictional forces

In this subsection, the coefficient of friction is set to $\mu = 0.0$. The area fraction of the system is $\phi = 0.82$, and the diameter of the intruder is taken as $D_i = 0.05$ m. The drag force increases with an increase in the fraction of dumbbells in a frictional system, as seen in the inset of Fig. 2(a). Surprisingly, in a frictionless system, we noticed an anomalous behavior in the intruder's drag [Fig. 7(a)], and in a sense, the drag is almost independent of the fraction of dumbbells. The tangential forces between the particles are primarily responsible for the interlocking type of phenomena exhibited by the dumbbells. In a frictionless system, the tangential forces are absent, and hence the ability of the dumbbells to show interlocking type of phenomena is negligible. Therefore, in such systems, the drag experienced by the intruder is not significantly affected by the fraction of dumbbells. This result reveals that the effect of the particle geometry on the drag dynamics of the intruder can be witnessed only in a frictional system. To this end, we point out that it is difficult to isolate the sole effect of the geometry of the particles on the intruder's drag as the geometry and the frictional forces between the particles seem to be interrelated [11]. In addition, the drag force experienced by the intruder in a frictional system is 3 ($db_{frac} = 0.0$) to 9 ($db_{frac} = 1.0$) times higher than that of

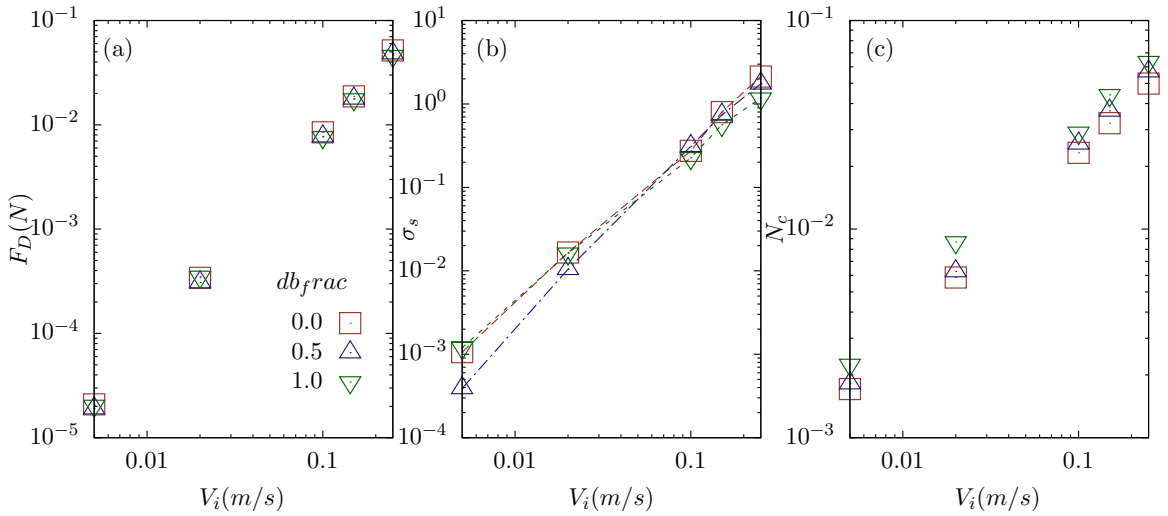

FIG. 7. (a) The time-averaged drag force F_D, (b) the stress decline slope σ_s, and (c) the averaged number of particles in contact (N_c) as a function of intruder's velocity V_i for the fractions of dumbbells (db_{frac}) = 0, 0.5, and 1. The coefficient of friction is $\mu = 0.0$, the area fraction is $\phi = 0.82$, and the diameter of the intruder is $D_i = 0.05$ m.

the frictionless system. This can be attributed to the size of the cluster of particles in front of the intruder. In the sense, the cluster size is smaller for a frictionless system as compared to that of the frictional system. The tangential forces which are mainly responsible for the evolution of clusters in front of the intruder are absent in a frictionless system leading to smaller cluster size. It was previously noticed that the friction between the contacting particles increases the inherent stability and formation of strong force chains [29], thus supporting our claim regarding the cluster size. The stress decline slope varies insignificantly with the fraction of dumbbells [Fig. 7(b)] at all intruder velocities. This is due to the minimal effect of an interlocking type of phenomena among dumbbells in a frictionless system, as explained above. Due to the same reason, the average number of contacts of the intruder remains almost the same for the entire fraction of dumbbells [Fig. 7(c)], unlike a significant difference that has been noticed in the case of a frictional system [Fig. 2(c)]. The results obtained from the frictional and the frictionless system reveal that the frictional interactions between the particles play a major role in the drag dynamics of an intruder. One of the major factors which determine the number of frictional interactions is the area fraction of the system. In the next subsection, we will address the effect of the area fraction of the system on the intruder's drag.

C. Area fraction

In this subsection, we analyze how the dynamics of an intruder and its surroundings is affected by the area fraction of the system comprising dumbbells and disks. The area fraction (ϕ) of the system is computed as

$$\phi = \frac{A_g}{A_s - A_i}. \tag{3}$$

Here A_g is the total area occupied by granular particles, A_s is the area of our system, and A_i is the area of the intruder. The area fraction of the system $\phi = 0.43$, 0.77, and 0.82 is achieved by using 100 000, 180 000, and 188 000 granular particles, respectively, while fixing the system dimensions the same for all the cases. Note that in this subsection, the fraction of dumbbells is $db_{frac} = 0.5$, the coefficient of friction is set to $\mu = 0.5$, and the diameter of the intruder is taken as $D_i = 0.05$ m. The frictional forces come into play when two particles interact with each other in a granular medium. As may be expected, a system with a higher area fraction will have a larger number of frictional interactions among the particles. Apart from an increase in the frictional interactions, a denser granular system results in the evolution of stronger force chain networks that offer greater resistance to the movement of an object through the granular medium [30–32]. These could be the reasons for an increase in the drag force with an increase in the area fraction for all the fractions of dumbbells [Fig. 8(a)]. The drag force on the intruder for $\phi = 0.82$ is ten times more than what it experiences in a system with $\phi = 0.43$. So one can infer that, in a denser system, the intruder exerts greater stress on the particles in front of it. Consequently, the stress decline slope increases with an increase in the area fraction [Fig. 8(b)]. Interestingly, the drag force on the intruder is noticed to scale as the square of its velocity V_i irrespective of the area fraction of the system. Moreover, the number of contacts of the intruder increases with an increase in the area fraction [Fig. 8(c)], which results in higher stress or, in other words, a higher drag force experienced by the intruder.

D. Diameter of the intruder

The effect of various parameters of the system on the drag dynamics of the intruder has been discussed in the previous subsections. In this subsection, we are going to elucidate the drag dependence on the intruder's geometry. To this end, we analyzed the system for five different diameters of the intruder, starting from the size of the disk (d) and ranging up to $10d$. For all cases, the fraction of dumbbells is $db_{frac} = 0.5$, the area fraction of the system is set to $\phi = 0.77$, and the

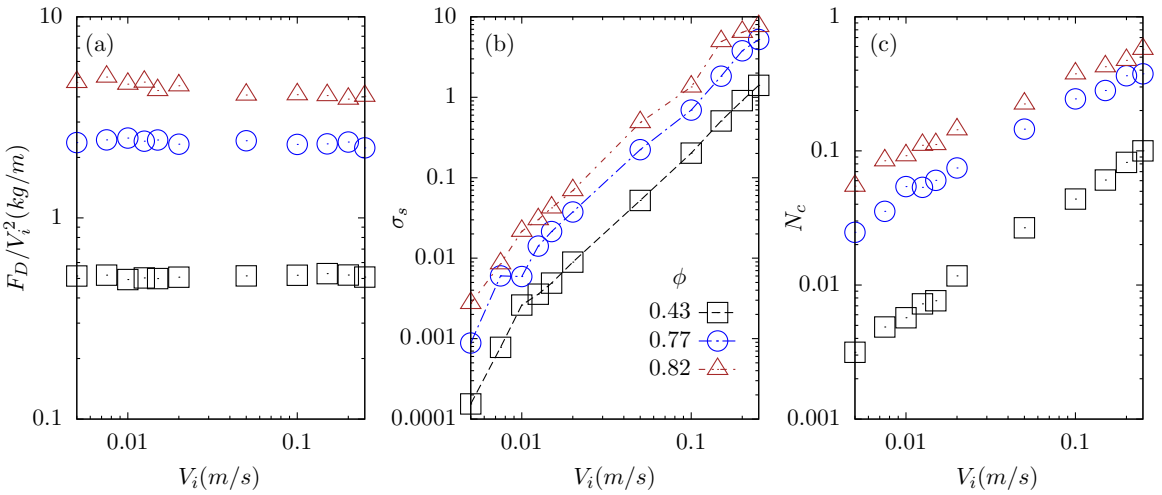

FIG. 8. (a) The time-averaged drag force F_D, (b) the stress decline slope σ_s, and (c) the number of contacts (N_c) as a function of the intruder's velocity V_i for systems with an area fraction of (ϕ) = 0.43, 0.77, and 0.82. The fraction of dumbbells (db_{frac}) is 0.5, the diameter of the intruder (D_i) is 0.05 m, and the coefficient of friction (μ) is 0.5.

coefficient of friction is $\mu = 0.5$. The drag force increases as the diameter of the intruder (D_i) increases, as shown in Fig. 9(a). This is due to an increase in the size of the structure of particles in front of the intruder with an increase in D_i. The reason for this is as D_i increases, the surface of the intruder available for the particles in front of it to form a structure increases, which increases the size of the structure. Similar behavior of an increase in the drag force experienced by the intruder with an increase in the intruder's diameter was noticed in both the confined [10] as well as the nonconfined [5,33] granular media. The drag force is noticed to scale as the square of the intruder's velocity V_i^2 [see Fig. 9(a)]. Moreover, the magnitude of drag force experienced by an intruder having a diameter of $D_i = 0.1$ m is on average six times more than that of the one having $D_i = 0.01$ m. Interestingly, when we plot the drag force normalized by the intruder's diameter as a function of velocity V_i [Fig. 9(b)], all the data collapse onto a single curve. This indicates that the drag force scales as the diameter of the intruder. Figure 9(c) shows that the stress decline slope increases as the intruder diameter increases. This result suggests that the stress experienced by the particles close to the intruder surface increases with an increase in intruder diameter (D_i) due to an increase in the drag force. However, the distance from the intruder at which the stress is equal to the average stress of the system doesn't vary significantly with D_i. Therefore, the stress decline slope increases with an increase in D_i. An increase in the intruder's diameter increases the surface available for the surrounding particles to get in contact with it. This yields an increase in the number of contacts with an increase in the intruder's diameter [Fig. 9(d)].

E. Mean flow fields

We have generated time-averaged flow fields by using discrete microscopic data such as velocities, positions, and stress of each of the particles in a designated region around the intruder. The Gaussian coarse-graining function, as implemented by Glasser and Goldhirsch [34], is used to calculate the parameters such as the area fraction $\phi(t)$, velocity $v(t)$, stress tensor $\boldsymbol{\sigma}_{ij(t)}$, and pressure $P(t)$ at a spatial location p with a position vector $\boldsymbol{r_p}$ and at an arbitrary time t as

$$\phi(t) = \left[\sum_{i=1}^{n} \frac{\pi d_i^2}{4} \mathcal{W}(\boldsymbol{r_p} - \boldsymbol{r_i(t)})\right], \tag{4}$$

$$\boldsymbol{v}(t) = \left[\sum_{i=1}^{n} \frac{\pi d_i^2}{4} \boldsymbol{v_i} \mathcal{W}(\boldsymbol{r_p} - \boldsymbol{r_i(t)})\right]/\phi, \tag{5}$$

$$\boldsymbol{\sigma_{ij}}(t) = \sum_{i=1}^{n} \sum_{j=i+1}^{n} (\boldsymbol{F^{ij}} \boldsymbol{r_{ij}}) \int_{s=0}^{1} \mathcal{W}(\boldsymbol{r_p} - \boldsymbol{r_i(t)} + s\boldsymbol{r_{ij}})\, ds, \tag{6}$$

$$P(t) = \frac{-\mathrm{tr}[\sigma_{ij}(t)]}{2}, \tag{7}$$

$$\mathcal{W}(\boldsymbol{r}) = \frac{1}{\pi w^2} e^{-\boldsymbol{r}^2/w^2}. \tag{8}$$

Here $\mathcal{W}(\boldsymbol{r})$ is the coarse-graining function, and d_i and $\boldsymbol{r_i(t)}$ are the diameter and the position vector of the particle i, respectively. The i and j correspond to disks or each constituent part of a dumbbell, and n is the total number of disks and constituent parts of a dumbbell. $\boldsymbol{F^{ij}}$ is the force on the particle i due to particle j, and $\boldsymbol{r_{ij}}$ is a vector in the direction of line joining the centers of two particles i and j. Moreover, $w = 1.0$ and $\mathcal{W}(\boldsymbol{r_p} - \boldsymbol{r_i}) = 0$ if $|\boldsymbol{r_p} - \boldsymbol{r_i}| > 3w$, and ϕ, $\boldsymbol{v}$, and P are the time-averaged area fraction, velocity, and pressure, respectively. The presented flow fields correspond to a circular region of radius 0.15 m ($\sim 15 \times d$), whose center is at the center of the intruder, and are time-averaged over 10 000 frames. Here d denotes the average diameter of the disk. The system size, however, is much bigger than the above-mentioned region. Typically the effect of the motion of the intruder on the granular particles occurs locally within this distance, and these results are shown to highlight the effect of the intruder's motion on the dynamics of surrounding granular particles. In the present study, we considered a large enough simulation system such that the drag force on the intruder is independent of the system size, and we made sure that the walls and periodic boundary are not significantly influencing

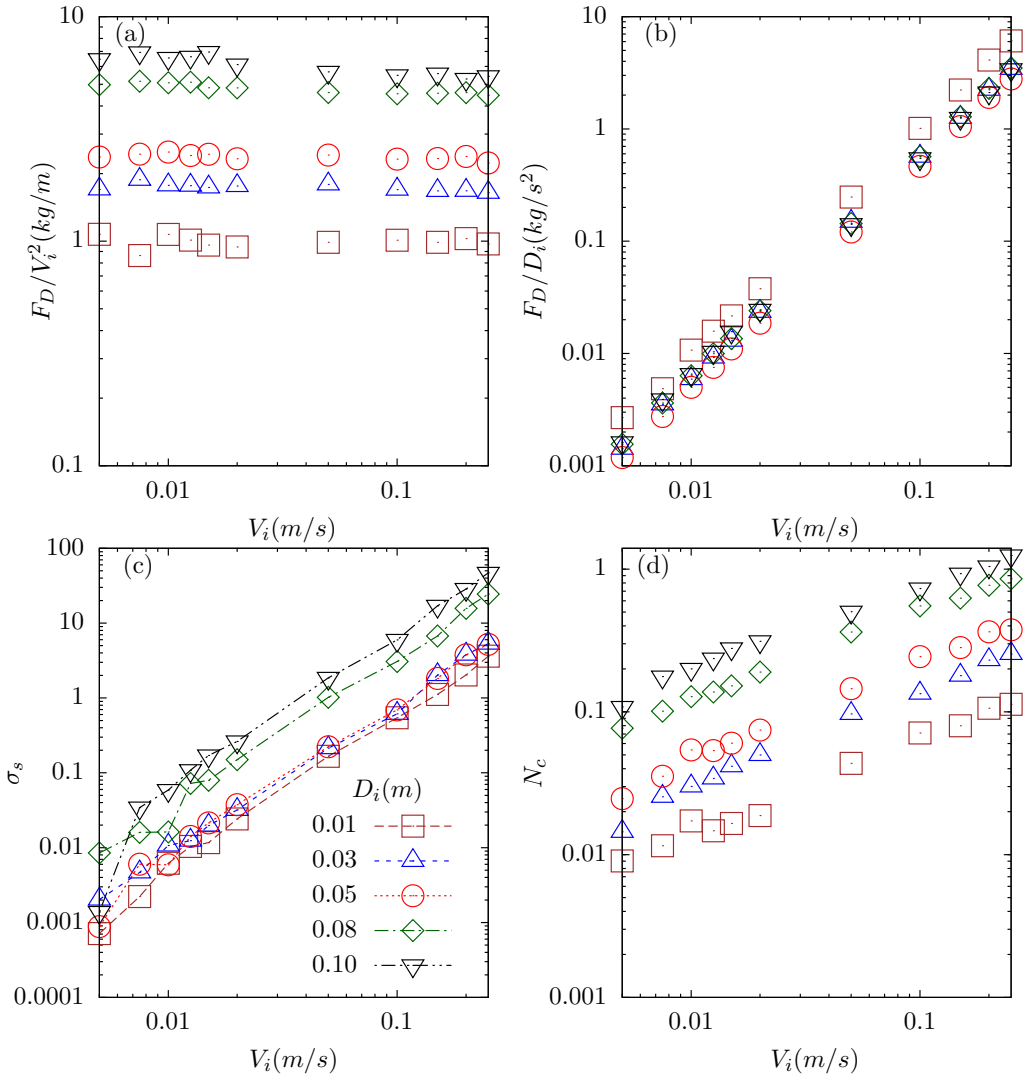

FIG. 9. (a) The time-averaged drag force F_D, (b) the drag force normalized by the intruder's diameter (F_D/D_i), (c) the stress decline slope σ_s, and (d) the number of particle contacts (N_c) as a function of the intruder's velocity V_i for different diameters of the intruder (D_i). The fraction of dumbbells (db_{frac}) is 0.5, the area fraction of the system (ϕ) is 0.77, and the coefficient of friction (μ) is 0.5.

the dynamics of the intruder (the intruder is kept far away from the wall).

Figures 10(a), 10(b), and 10(c) illustrate the time-averaged pressure fields for the fraction of dumbbells $db_{frac} = 0.0$, 0.5, and 1.0, respectively. At all fractions of dumbbells, the pressure is maximum near the front surface of the intruder. Moreover, a high-stress zone (the regions in red are noticed in front of the intruder due to the formation of a cluster of particles as we have explained earlier. The pressure decreases as the distance from the intruder's front surface increases. The reason for this behavior is that the intruder can transmit stress to only the particles lying closer to it because ours is a gravityless system. Figures 10(d), 10(e), and 10(f) show the velocity V fields for $db_{frac} = 0.0$, 0.5, and 1.0, respectively. The zones in red in front of the intruder are noticed in velocity fields as well, which further confirms the presence of the cluster. Moreover, the velocities of particles in front of the intruder increase with an increase in the fraction of dumbbells. This can be attributed to an increase in the interlocking type of phenomena where a certain type of particle contacts (Fig. 3) involving dumbbells resist their relative motion. Figures 10(g)–(i) display the mean flow fields of shear stress $|\sigma_{xy}|$ for different fractions of dumbbells. Here $|\sigma_{xy}|$ is the magnitude of shear stress. The particles whose y position is almost equal to that of the intruder's y position does not detour around it; instead, they move ahead along with it. This results in the absence of shear stress at $y = 0.0$. Due to the movement of the intruder, the particles near the front surface of it, other than the ones mentioned above, are impelled to detour around it. This creates a relative motion between the contacting particles around the surface of the intruder. Consequently, high shear stress is experienced by these particles, which correspond to the regions in deep red. However, this phenomenon is not significant at positions far away from the intruder as there is hardly any relative motion between the particles. Shear stress is almost zero in the regions above and below the intruder as the particles in those regions are unaffected by its movement because our system is a gravityless one.

Figures 11(a), 11(b), and 11(c) show the mean pressure fields at the diameters of the intruder $D_i =$ 0.01 m,

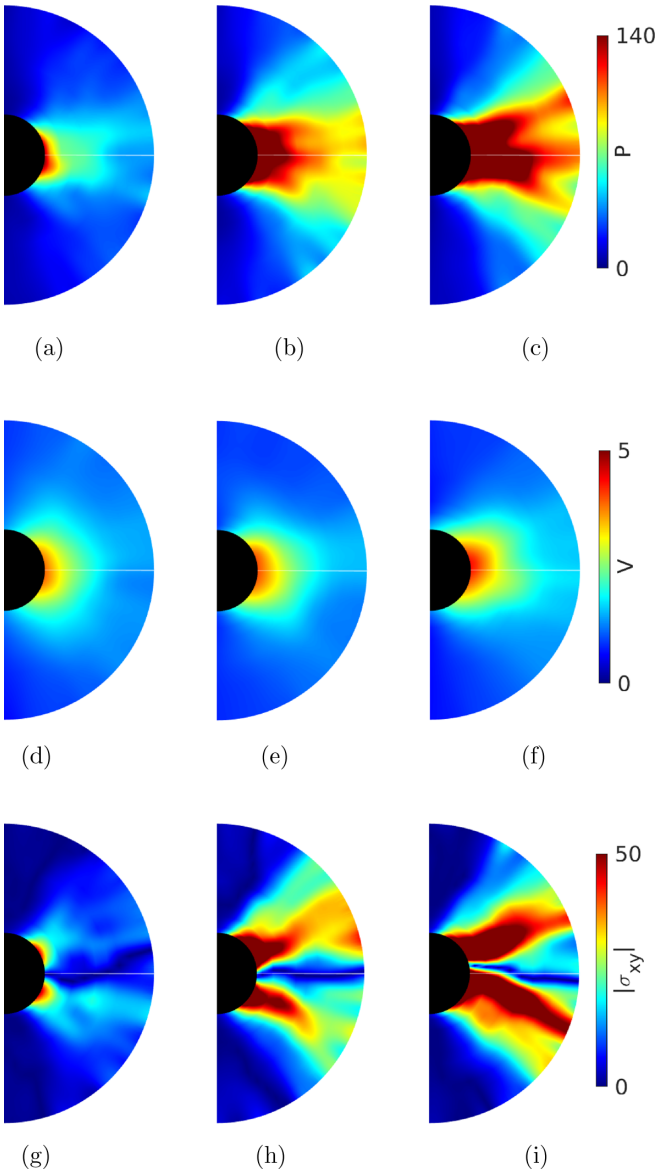

FIG. 10. The time-averaged flow fields for depicting pressure P (N/m^2), velocity V (m/s), and shear stress $|\sigma_{xy}|$ (N/m^2) in front of the intruder for different fractions of dumbbells (db_{frac}): (a), (d), (g) 0.0, (b), (e), (h) 0.5, and (c), (f), (i) 1.0. The modulus of σ_{xy} indicates the magnitude of shear stress. The diameter of the intruder is $D_i = 0.05$ m, $V_i = 0.05$ m/s, the coefficient of friction $\mu = 0.5$, and the area fraction (ϕ) of the system is 0.82.

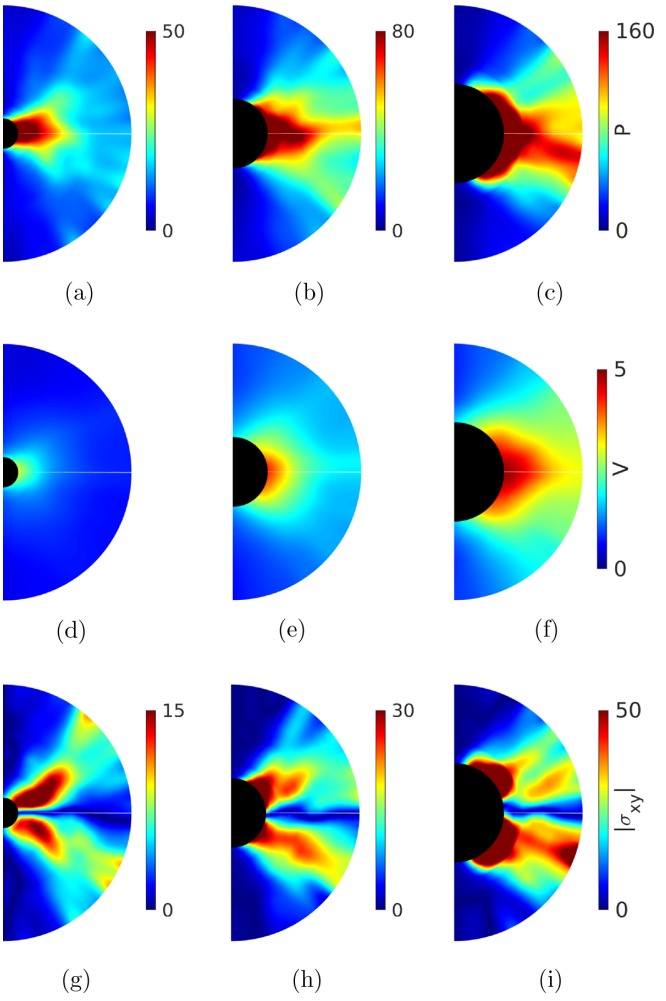

FIG. 11. The time-averaged flow fields for depicting pressure P (N/m^2), velocity V (m/s), and shear stress $|\sigma_{xy}|$ (N/m^2) in front of the intruder for different intruder diameters (D_i): (a), (d), (g) 0.01 m, (b), (e), (h) 0.05 m, and (c), (f), (i) 0.10 m. The velocity of the intruder is $V_i = 0.05$ m/s, $\mu = 0.5$, $\phi = 0.77$, and the fraction of dumbbell (db_{frac}) in the system is 0.5.

0.05 m, and 0.10 m, respectively, for $db_{frac} = 0.5$. As the intruder diameter increases, the high-stress zone expands in front of it. This is because the larger the intruder surface available, the larger the size of the cluster it can hold in front of it, particularly in the y direction. The regions in red in the velocity fields increases with an increase in D_i [Figs. 11(d)–11(f)]. This result supports our claim that the size of the cluster increases with an increase in the intruder's diameter. The velocities of the particles on the front surface of the intruder experience the same velocity as that of the intruder. The velocity reduces gradually as the distance from the intruder increases due to a decrease in the stress transmission as noticed in Fig. 11(a). As the diameter of the moving intruder increases, more layers of particles in front of it are forced to detour around a larger distance and then get detached from it. This yields a relative motion among the particles at different radial distances from the intruder's center. Consequently, the shear stress increases with an increase in the diameter of the intruder [see Figs. 11(g)–11(i)]. In the Supplemental Material [28] we have also shown the flow fields of $\phi = 0.82$ with $\mu = 0.0$ for different dumbbell fraction (shown in Fig. S4), Fig. S5 shows the flow fields for $\phi = 0.77$, $\mu = 0.5$, and Fig. S6 for $db_{frac} = 0.5$, $\mu = 0.5$ at different area fraction.

IV. CONCLUSION

In this work we studied the dynamics of a moving intruder and its effect on a mixture of dumbbells and disks in the absence of gravity. To this end, we studied the effect of parameters such as the fraction of dumbbells, area fraction,

and the intruder's diameter and its velocity. The drag force on the intruder moving through granular media increases with an increase in the fraction of dumbbells at constant area fraction. This is due to an additional resistance offered by the dumbbells apart from the interparticle friction. Surprisingly, the so-called additional resistance seems to be insignificant in the absence of interparticle friction. In a sense, the drag force is independent of the fraction of dumbbells in a frictionless system. Another interesting result is the drag force on an intruder scales as the square of its velocity irrespective of the fraction of dumbbells (V_i is in the range of 0.001 m/s to 0.25 m/s), the area fraction of the system, or the intruder's diameter. Furthermore, we presented the mean flow fields to show the response of the granular media to a moving intruder. They revealed that the stress experienced by the particles in front of the intruder increases with an increase in the intruder's diameter. This is due to an increase in the size of the cluster of particles formed in front of it resulting from an increase in the intruder's surface. Moreover, as the diameter of the intruder increases, it forces the larger number of particles in front of it to detour around it. This results in greater shear stress experienced by the particles in front of the intruder.

[1] M. Dhiman, S. Kumar, K. A. Reddy, and R. Gupta, Origin of the long-ranged attraction or repulsion between intruders in a confined granular medium, J. Fluid Mech. **886**, A23 (2020).

[2] T. Furuta, S. Kumar, K. A. Reddy, H. Niiya, and H. Katsuragi, Packing-dependent granular friction exerted on a rod withdrawn from a granular layer: The role of shear jamming, New J. Phys. **21**, 023001 (2019).

[3] I. Albert, J. G. Sample, A. J. Morss, S. Rajagopalan, A.-L. Barabási, and P. Schiffer, Granular drag on a discrete object: Shape effects on jamming, Phys. Rev. E **64**, 061303 (2001).

[4] F. Q. Potiguar and Y. Ding, Lift and drag in intruders moving through hydrostatic granular media at high speeds, Phys. Rev. E **88**, 012204 (2013).

[5] R. Albert, M. A. Pfeifer, A.-L. Barabási, and P. Schiffer, Slow Drag in a Granular Medium, Phys. Rev. Lett. **82**, 205 (1999).

[6] C. Liu, H. Wan, and L. Wang, Effect of movement direction on resistance force in granular media, Powder Technol. **344**, 545 (2019).

[7] B. K. Tripura, S. Kumar, K. A. Reddy, and J. Talbot, Role of shape on the forces on an intruder moving through a dense granular medium, Part. Sci. Technol. **0**, 1 (2021).

[8] D. Wang, Y. Yang, and W. Du, The drag on a vibrated intruder moving in the confined granular media, Powder Technol. **286**, 385 (2015).

[9] F. Zhou, S. G. Advani, and E. D. Wetzel, Slow drag in polydisperse granular mixtures under high pressure, Phys. Rev. E **71**, 061304 (2005).

[10] F. Zhou, S. G. Advani, and E. D. Wetzel, Simulation of slowly dragging a cylinder through a confined pressurized bed of granular materials using the discrete element method, Phys. Fluids **19**, 013301 (2007).

[11] F. Zhou, S. G. Advani, and E. D. Wetzel, Simulation of the slow drag of a cylinder through a confined pressurized bed of dumbbell and elliptically cylindrical granules using the discrete element method, Comput. Model. Eng. Sci. **39**, 49 (2009).

[12] F. Zhou, S. G. Advani, and E. D. Wetzel, Characterization of the viscous behavior of compacted ceramic particles under shear and pressure loads, *Proceedings of the ASME 2003 International Mechanical Engineering Congress and Exposition. Materials*. Washington, DC, USA. November 15–21, 2003 (ASME, 2003), pp. 145–149.

[13] D. J. Costantino, J. Bartell, K. Scheidler, and P. Schiffer, Low-velocity granular drag in reduced gravity, Phys. Rev. E **83**, 011305 (2011).

[14] A. Seguin, A. Lefebvre-Lepot, S. Faure, and P. Gondret, Clustering and flow around a sphere moving into a grain cloud, Eur. Phys. J. E **39**, 63 (2016).

[15] A. Vamsi Krishna Reddy, S. Kumar, K. A. Reddy, and J. Talbot, Granular silo flow of inelastic dumbbells: Clogging and its reduction, Phys. Rev. E **98**, 022904 (2018).

[16] H. Kruggel-Emden, S. Rickelt, S. Wirtz, and V. Scherer, A study on the validity of the multi-sphere discrete element method, Powder Technol. **188**, 153 (2008).

[17] H. Pourtavakoli, E. J. R. Parteli, and T. Pöschel, Granular dampers: Does particle shape matter? New J. Phys. **18**, 073049 (2016).

[18] A. Vamsi Krishna Reddy, K. Reddy, S. Kumar, and K. A. Reddy, Granular particle-shape heterogeneous mixtures discharging through a silo, J. Fluid Mech. **912**, A22 (2021).

[19] S. Mandal and D. V. Khakhar, Dense granular flow of mixtures of spheres and dumbbells down a rough inclined plane: Segregation and rheology, Phys. Fluids **31**, 023304 (2019).

[20] P. A. Cundall and O. D. L. Strack, A discrete numerical model for granular assemblies, Géotechnique **29**, 47 (1979).

[21] N. V. Brilliantov, F. Spahn, J.-M. Hertzsch, and T. Pöschel, Model for collisions in granular gases, Phys. Rev. E **53**, 5382 (1996).

[22] L. E. Silbert, D. Ertaş, G. S. Grest, T. C. Halsey, D. Levine, and S. J. Plimpton, Granular flow down an inclined plane: Bagnold scaling and rheology, Phys. Rev. E **64**, 051302 (2001).

[23] A. P. Thompson, H. M. Aktulga, R. Berger, D. S. Bolintineanu, W. M. Brown, P. S. Crozier, P. J. in 't Veld, A. Kohlmeyer, S. G. Moore, T. D. Nguyen, R. Shan, M. J. Stevens, J. Tranchida, C. Trott, and S. J. Plimpton, LAMMPS - a flexible simulation tool for particle-based materials modeling at the atomic, meso, and continuum scales, Comp. Phys. Comm. **271**, 10817 (2022).

[24] A. Stukowski, Visualization and analysis of atomistic simulation data with OVITO-the Open Visualization Tool, Model. Simu. Mate. Sci. Eng. **18**, 015012 (2010).

[25] C. R. Wassgren, J. A. Cordova, R. Zenit, and A. Karion, Dilute granular flow around an immersed cylinder, Phys. Fluids **15**, 3318 (2003).

[26] J. E. Hilton and A. Tordesillas, Drag force on a spherical intruder in a granular bed at low Froude number, Phys. Rev. E **88**, 062203 (2013).

[27] S. Kumar, M. Dhiman, and K. A. Reddy, Magnus effect in granular media, Phys. Rev. E **99**, 012902 (2019).

[28] See Supplemental Material at http://link.aps.org/supplemental/10.1103/PhysRevE.106.014901 for the plots showing the time-averaged drag force, stress-decline slope σ_s, and average number of particles in contact as a function of intruder velocity for area fraction 0.43, 0.77 and additional plots showing force distribution and flow fields around the intruder surface.

[29] D. Barreto and C. O'Sullivan, The influence of interparticle friction and the intermediate stress ratio on soil response under generalised stress conditions, Granular Matter **14**, 505 (2012).

[30] L. Kondic, A. Goullet, C. S. O'Hern, M. Kramar, K. Mischaikow, and R. P. Behringer, Topology of force networks in compressed granular media, Europhys. Lett. **97**, 54001 (2012).

[31] P. Guo, Critical length of force chains and shear band thickness in dense granular materials, Acta Geotechnica **7**, 41 (2012).

[32] M. Kramár, A. Goullet, L. Kondic, and K. Mischaikow, Persistence of force networks in compressed granular media, Phys. Rev. E **87**, 042207 (2013).

[33] A. Panaitescu, X. Clotet, and A. Kudrolli, Drag law for an intruder in granular sediments, Phys. Rev. E **95**, 032901 (2017).

[34] B. J. Glasser and I. Goldhirsch, Scale dependence, correlations, and fluctuations of stresses in rapid granular flows, Phys. Fluids **13**, 407 (2001).